ORIGINAL PAPER

Structure of Tau filaments in Prion protein amyloidoses

Grace I. Hallinan[1] · Md Rejaul Hoq[2] · Manali Ghosh[2] · Frank S. Vago[2] · Anllely Fernandez[1] · Holly J. Garringer[1] · Ruben Vidal[1,3] · Wen Jiang[2] · Bernardino Ghetti[1]

Abstract

In human neurodegenerative diseases associated with the intracellular aggregation of Tau protein, the ordered cores of Tau filaments adopt distinct folds. Here, we analyze Tau filaments isolated from the brain of individuals affected by Prion-Protein cerebral amyloid angiopathy (PrP-CAA) with a nonsense mutation in the *PRNP* gene that leads to early termination of translation of PrP (Q160Ter or Q160X), and Gerstmann–Sträussler–Scheinker (GSS) disease, with a missense mutation in the *PRNP* gene that leads to an amino acid substitution at residue 198 (F198S) of PrP. The clinical and neuropathologic phenotypes associated with these two mutations in *PRNP* are different; however, the neuropathologic analyses of these two genetic variants have consistently shown the presence of numerous neurofibrillary tangles (NFTs) made of filamentous Tau aggregates in neurons. We report that Tau filaments in PrP-CAA (Q160X) and GSS (F198S) are composed of 3-repeat and 4-repeat Tau isoforms, having a striking similarity to NFTs in Alzheimer disease (AD). In PrP-CAA (Q160X), Tau filaments are made of both paired helical filaments (PHFs) and straight filaments (SFs), while in GSS (F198S), only PHFs were found. Mass spectrometry analyses of Tau filaments extracted from PrP-CAA (Q160X) and GSS (F198S) brains show the presence of post-translational modifications that are comparable to those seen in Tau aggregates from AD. Cryo-EM analysis reveals that the atomic models of the Tau filaments obtained from PrP-CAA (Q160X) and GSS (F198S) are identical to those of the Tau filaments from AD, and are therefore distinct from those of Pick disease, chronic traumatic encephalopathy, and corticobasal degeneration. Our data support the hypothesis that in the presence of extracellular amyloid deposits and regardless of the primary amino acid sequence of the amyloid protein, similar molecular mechanisms are at play in the formation of identical Tau filaments.

Keywords GSS · PrP-CAA · Tau · APrP · Cryo-EM · Neurodegeneration

These authors jointly supervised this work: Ruben Vidal, Wen Jiang, Bernardino Ghetti.

Grace I. Hallinan and Rejaul Hoq contributed equally to this work.

✉ Ruben Vidal
 rvidal@iupui.edu

✉ Wen Jiang
 jiang12@purdue.edu

✉ Bernardino Ghetti
 bghetti@iupui.edu

[1] Department of Pathology and Laboratory Medicine, Indiana University School of Medicine, Indianapolis, IN 46202, USA

[2] Department of Biological Sciences, Markey Center for Structural Biology, Purdue University, West Lafayette, IN 47906, USA

[3] Stark Neurosciences Research Institute, Indiana University School of Medicine, Indianapolis, IN 46202, USA

Introduction

Neurodegenerative diseases with Tau pathology may present with diverse clinical symptoms and have distinct neuropathologies [20]. In fact, in addition to differences in the involvement of anatomic areas and affected cell types, Tau aggregates may also differ in Tau isoform composition and the structure of the Tau filament [3, 10–12, 16, 64]. In the adult brain, alternative mRNA splicing of exons 2, 3, and 10 of the *Microtubule-Associated Protein Tau* (*MAPT*) gene yields six Tau isoforms that differ by the absence or presence of one or two acidic N-terminus inserts, and whether they contain three or four repeats (3R, 4R) of a conserved tubulin binding motif at the C-terminus [25]. All six isoforms are found in the insoluble Tau deposits of Alzheimer disease (AD) and chronic traumatic encephalopathy (CTE), whereas only 3R-Tau isoforms are found within those of Pick

disease (PiD) and only 4R-Tau isoforms in the deposits of other diseases such as progressive supranuclear palsy (PSP) and corticobasal degeneration (CBD) [20, 24, 26, 27]. Using cryo-electron microscopy (cryo-EM), it has been recently determined that the fold of the core of Tau filaments in sporadic and familial AD differs from those in PiD and CBD [3, 10–12, 16, 64]. Furthermore, although neurofibrillary tangles (NFTs) in AD, CTE, and primary age-related tauopathy (PART) [6, 8, 43] incorporate all six Tau isoforms, the fold of the core of Tau filaments is identical in AD and PART and different from that in CTE [12, 16, 55]. Thus, the Alzheimer Tau fold may be found in the presence (AD) or in the absence (PART) of amyloid β (Aβ); however, the specific role of Aβ in the pathogenesis of Tau aggregation in AD remains undetermined. In addition, whether the conformation and filament fold of Tau varies in NFTs from other neurodegenerative diseases in which the primary amyloid protein deposited is not Aβ [21–23, 59, 60] has yet to be determined.

The Prion-Protein Amyloidoses are dominantly inherited diseases, associated with missense, nonsense, and insertion mutations in the *PRNP* gene [22]. The co-existence of parenchymal PrP amyloid (APrP) with intraneuronal Tau aggregates has been shown to occur consistently in association with some *PRNP* mutations [22]; however, in Gerstmann–Sträussler–Scheinker disease (GSS) associated with the P102L mutation, the neuropathologic phenotype has consistently shown present of APrP but not Tau aggregates in neurons [22]. In Prion-Protein Cerebral Amyloid Angiopathies (PrP-CAA), which are associated with nonsense mutations in the *PRNP* gene [21, 22, 37], the main histologic feature is the co-existence of numerous intraneuronal Tau aggregates with APrP in the vascular compartment. Whether the co-existence of intraneuronal Tau aggregates with intraparenchymal APrP amyloid is dependent of the conformation of the APrP found in the deposits remains to be established [20, 45].

The present work focuses on PrP-CAA with a c.478C > T mutation in *PRNP* that leads to a truncated PrP protein (p.Q160Ter or Q160X) [17, 37], and GSS with a c.593T > C mutation in *PRNP* that leads to an amino acid substitution in PrP (p.F198S) [36]. In these two forms of amyloidosis [referred herein as PrP-CAA (Q160X) and GSS (F198S)], APrP coexists with numerous Tau neurofibrillary aggregates made of 3R- and 4R-Tau isoforms, suggesting that different amyloids may share pathogenetic mechanisms leading to Tau aggregation in AD, PrP-CAA, and GSS. Importantly, the anatomical distribution of the respective amyloid protein differs significantly between PrP-CAA, GSS, and AD [21, 22].

Herein, we determined for the first time the biochemical properties and atomic structures of Tau in PrP-CAA (Q160X) and GSS (F198S). This work represents a significant step towards the demonstration of the existence of different conformers of Tau in neurodegenerative diseases with Tau pathology and our understanding of the role of amyloid in the pathogenic mechanism(s) of neurodegeneration.

Materials and methods

Neuropathology

Neuropathology was carried out as previously described [21, 49]. Please see Supplementary Material Methods section for detailed information regarding clinical, genetic, and neuropathologic findings. One half of the brain was fixed in formalin and the other half was frozen at − 80 °C. Hemispheric coronal slabs were selected that included areas of the frontal, insular, temporal, parietal, and occipital lobes. These were submitted for histology and immunohistochemistry. Tissue samples were also obtained from representative brain regions. Brain sections were 8-μm thick and were counterstained with hematoxylin. Thioflavin S (Th-S) was used to demonstrate the presence of amyloid deposits and neurofibrillary tangles. For immunohistochemical studies, primary antibodies (Table S2) were AT8 (Thermo Fisher Scientific MN1020, 1:300), Abeta (NAB 228); anti PrP (Ab 95–108, 1:300); HT7 (1:1000), RD3 (Merck 05–803, 1:3,000), and RD4 (Upstate, 1:100). Double immunohistochemical studies were performed using the Dako En-Vision Doublestain System (Dako) following the manufacturer's instructions.

Sanger DNA analysis

Genomic DNA was extracted from frozen brain tissue. Polymerase chain reaction (PCR) was performed for the amplification of the *PRNP* and *AβPP* genes as described [44, 51]. PCR products were sequenced on a CEQ 2000XL DNA analysis system (Beckman Coulter, Fullerton, CA).

Whole-exome sequencing (WES)

Target enrichment made use of the SureSelectTX human all-exon library (V6, 58 megabase pairs; Agilent) and high-throughput sequencing was carried out using a HiSeq 4,000 (sx75 base-pair paired-end configuration; Illumina). Bioinformatics analyses were performed as described [14].

Tau extraction

Sarkosyl-insoluble Tau was extracted from gray matter of fresh-frozen frontal cortex as previously described [26]. Briefly, 6 g of tissues were homogenized in A68 extraction

buffer consisting of 10 mM Tris–HCl, pH 7.4, 0.8 M NaCl, 1 mM EGTA, 5 mM EDTA, and 10% sucrose with protease and phosphatase inhibitors. After a centrifugation at $20,000 \times g$, the supernatants were brought to 1% sarkosyl and incubated at room temperature (RT) while shaking. The supernatants were spun at $100,000 \times g$ for 1 h at 4 °C, and the sarkosyl-insoluble pellets were resuspended in 10 μl/g tissue 50 mM Tris–HCl, pH 7.4. This resuspended pellet was further purified by 30-fold dilution in A68 extraction buffer, followed by centrifugation at $20,000 \times g$ for 30 min at 4 °C. The pellet, containing large contaminants, was discarded, and the supernatant was centrifuged at $100,000 \times g$ for 1 h at 4 °C. The final pellet was resuspended in 20 mM Tris–HCl, pH 7.4, and 100 mM NaCl, and stored at 4 °C.

Western blotting and dot-blot

For Western blotting, samples were resolved on 10% Tris–glycine gels (Bio-Rad) and blocked in 5% milk in TBS plus 0.1% Tween 20. For dot blots, 2 μl of diluted samples were dotted and absorbed onto 0.22 μm pore size nitrocellulose membranes (Santa Cruz), and then blocked in 5% milk in TBS plus 0.1% Tween 20. Primary antibodies were diluted in TBS plus 0.1% Tween 20 at the following dilutions: AT8 (Thermo Fisher, 1:1000), HT7 (Thermo Fisher, 1:1000), BR133, BR134 and BR135 (1:4000), RD3 and RD4 (Millipore, 1:1000), and 3F4 (Millipore, 1:1000).

Immuno-electron microscopy (EM)

Immunogold labeling was carried out as previously described [26]. Briefly, a 1 μl droplet of 1:50 insoluble tau fraction diluted in PBS was pipetted onto carbon nickel TEM grids (300 mesh, Ted Pella) and blotted dry after 2 min. The grid was blocked in 0.1% gelatin in PBS for 20 min, and then, excess solution blotted off with filter paper. Primary antibody diluted 1:50 in 0.1% gelatin in PBS was added for 1 h at RT. Grids were washed three times in 0.1% gelatin in PBS for 5 min each wash. Grids were then incubated in secondary antibody diluted 1:40 in 0.1% gelatin in PBS for 1 h at RT. Secondary antibodies used were 6 nm anti-mouse immunogold particles or 10 nm anti-rabbit immunogold particles (Electron Microscopy Sciences). Secondary antibody was washed off 3 times in 0.1% gelatin in PBS and blotted dry. Negative staining was performed with NanoVan (Ted Pella) for 5 s at RT. Pronase treatment of fibrils was carried out as described [26]. Briefly, a 5 μl solution of 0.4 mg/ml pronase was dropped onto the grid, and incubated for 5 min at RT. The pronase solution was wicked off with filter paper, and then, 0.1% gelatin solution was added to the grid for blocking. Primary and secondary antibody incubations were carried out as described above. Images were taken on

a Tecnai G2 Spirit Twin scope equipped with an AMT CCD Camera.

Tau seeding assay

Tau seeds were prepared from fresh-frozen brain tissue of AD Case 2, GSS (F198S) Case 2, and PrP-CAA (Q160X) case. Tissue was thawed and homogenized in 9 volumes of buffer consisting of 10 mM Tris–HCl, pH7.4, 0.8 M NaCl, and 0.1% sarkosyl, with protease and phosphatase inhibitors. Following a 10 min spin at $10,000 \times g$ at 4 °C, the supernatants were brought to 1% sarkosyl and incubated for 1 h at RT while shaking. The supernatants were spun at $300,000 \times g$ for 1 h, and the sarkosyl-insoluble pellets were resuspended in 0.1 ml PBS/gram tissue. The resuspended pellets were sonicated with a probe sonicator at 75 W, for a total of 25×500 ms pulses. The probe was cleaned with isopropanol and water between samples. This resuspended pellet was then centrifuged at $100,000 \times g$ for 30 min at 4 °C. The pellet was resuspended in 20 μl/gram tissue and sonicated again as before. Following a 10 min centrifugation at $10,000 \times g$ at 4 °C, the supernatant was removed and stored at –80 °C until used as seeds on cells. HEK 293 T cells stably expressing the aggregation prone repeat domain of Tau with the disease associated P301S mutation, fused at the C-terminus to either CFP or YFP, were obtained from ATCC [33]. Cells were cultured in DMEM supplemented with 10% FBS, 1% pen/strep, and 1% GlutaMax (Invitrogen). Cells were plated at a density of 50,000 cells/well in a 12-well plate, onto coverslips treated with 0.1 mg/ml poly-D-lysine for fixed cell imaging. Cells were incubated overnight at 37 °C and 5% CO_2. The following day, 1 μl seed material was combined with Lipofectamine 2000 (Thermo Fisher) and OptiMem medium, and incubated for 20 min at room temp. This transduction complex was then added onto the biosensor cells. Cells were incubated as before for 24–48 h. Cells were then washed with 1X PBS, fixed in 4% paraformaldehyde in PBS, and mounted onto microscope slides for imaging. Images were merged and cropped using ImageJ [53].

Mass spectrometry sample preparation

8 M urea, 50 mM Tris–HCl pH 8.5 (100 μl) was added to 20 μl of insoluble Tau fractions. The sample was reduced with 5 mM Tris(2-carboxyethyl)phosphine hydrochloride (TCEP) and alkylated with 10 mM chloroacetamide (CAM). The sample was diluted with 100 mM Tris–HCl to a final urea concentration of 2 M and digested overnight with 2 μg Trypsin/Lys-C Mix Mass Spectrometry (1:100 protease:substrate ratio, Promega Corporation). Peptides were desalted on a 50 mg Sep-Pak® Vac (Waters Corporation) employing a vacuum manifold (Waters Corporation). After elution from the column in 70% acetonitrile, 0.1%

formic acid (FA), peptides were dried by speed vacuum, resuspended in 40 μL of 0.1% FA, and filtered through a 0.2 μm spin filter (Millipore).

Nano-LC–MS/MS analysis

Nano-LC–MS/MS analyses were performed on an EASY-nLC HPLC system (Thermo Fisher Scientific) coupled to an Orbitrap Fusion Lumos mass spectrometer (Thermo Fisher Scientific). One quarter of the sample was loaded onto a reversed phase PepMapTM RSLC C18 column (2 μm, 100 Å, 75 μm × 25 cm) with Easy-Spray tip at 450 nl/min. Peptides were eluted from 3 to 30% B over 85 min, 30 to 80% B over 3 min, 80 to 4% B for 4 min (Mobile phases A: 0.1% FA, water; B: 0.1% FA, 80% Acetonitrile). Mass spectrometer settings include capillary temperature of 300 °C and ion spray voltage was kept at 1.9 kV. Replicate injections were run with the same LC and source methods (CID mode and EtHCD/HCD mode). For the CID method, the mass spectrometer method was operated in positive ion with a 3 s cycle time data-dependent acquisition method with advanced peak determination and Easy-IC (internal calibrant). Precursor scans (m/z 400–1500) were done with an Orbitrap resolution of 120,000, RF lens% 30, maximum inject time 50 ms, 4e5 normalized AGC target, including charges of 2–7 for fragmentation with an intensity threshold of 5e3, and 60 s dynamic exclusion. CID MS2 scans were performed in the ion trap at rapid speed with a 1.6 m/z isolation window, 35% normalized CID collision energy, 2e3 AGC target, and 35 ms maximum IT. The same precursor scan settings were used for the DDA EtHCD/HCD decision tree method, but with a minimum intensity filter of 1e5. The decision tree consisted of either HCD assisted ETD or HCD (30%) activation of charge states, 3, 4, 5, and 6–8 with 2 m/z isolation window, 35 ms max IT, and 1e4 AGC target in rapid ion trap mode. The data were recorded using Thermo Fisher Scientific Xcalibur software (Thermo Fisher Scientific Inc. 2017). Data were analyzed using PEAKS X + Studio [58], including all PTMs and mutations in SPIDER search.

Negative staining for cryo-electron microscopy

Negative stain embedded imaging of Tau fibrils was carried out by applying 3 μl of sample on affinity materials coated lacey carbon grid and incubated for 30 min, then washed 5 times with DI water, followed by addition of 1% uranyl acetate (UA). Then, UA was washed, blotted out and the grid was dried in air for 4–5 min. All negatively stained images were collected on a Tecnai-12 electron microscope.

Graphene oxide coating on Grid

A pyrene solution was used to cover the entire TEM grid surface with a single layer of graphene oxide. This was achieved using a two-step sequence of pyrene solution coating (3 μl of 0.1 mg/ml) that was applied to the dull side of a lacey TEM grid (Ted Pella #01824) followed by 3 μl of 0.1 mg/ml graphene oxide that was applied just before the pyrene solution dried out. The grid was then incubated for 2 min before the dull side of the grid was washed three times with DI water and the shiny side was washed one time with a 3 μl droplet of DI water before drying and storing the hydrophilic grids for pyrene-mediated antibody coating.

Affinity capture and grid freezing

Grids for cryo-EM were prepared using the Affinity Grid technique. A multi-arm Pyrene-PEG-Antibody conjugate was synthesized. Then, a 4 μl solution of Pyrene-PEG-Antibody was applied on a GO-coated grid, incubated for 5 min, and washed three times with Tris buffer. 2.5 μl of Tau sample was applied on the antibody coated side of the grid and incubated for 30 min, and washed 5 times with Tris buffer. The final volume of liquid on the grid was adjusted to ~3 μl before blotting for 3 s, followed by plunge freezing into liquid ethane on a cryo-plunger 3 (Gatan) in a biosafety hood.

High-resolution cryo-EM imaging

High-resolution cryo-EM images were collected on an FEI Titan Krios at 300 kV with a Gatan K3- detector in super-resolution mode. The inelastically scattered electrons were removed using a Gatan quantum energy filter with 20 eV slit width. For PrP-CAA (Q160X), we recorded 55 movie frames with an exposure time of 62 ms/frame, with a dose rate of 1.067 electrons per $Å^2$ per frame for a total accumulated dose of 53.35 electrons per $Å^2$ at a pixel size of 1.078 Å. For GSS (F198S), we recorded 50 movie frames with an exposure time of 62 ms/frame, and a dose rate of 1.067 electrons per $Å^2$ per frame for a total accumulated dose of 53.35 electrons per $Å^2$ at a pixel size of 1.078 Å. The datasets for PrP-CAA (Q160X) Tau and GSS (F198S) Tau are composed of 2004 and 1920 micrographs, respectively, with defocus values ranging from −0.5 to −2.5 μm. Corrections of super-resolution frames were done for gain reference, binned by a factor of 2, and then, frames were motion-corrected and dose-weighted using MotionCor2 [65]. The contrast transfer function (CTF) of all aligned and non-dose-weighted micrographs were estimated using Gctf [63].

Helical reconstruction

All subsequent image-processing was performed in RELION 3.1 software [31, 52]. Particles were picked manually using RELION helical picker as end-to-end segments. We extracted all the segments with a box size of 768 pixel (827 Å) to cover complete crossover, down scaled to 256 pixels to speed up analysis and an inter-box distance of ~ 10% of the box length. Several rounds of reference-free 2D classifications were carried out to find homogeneous subsets and remove junk particles using a regularization value of $T = 1–2$. PHFs and SFs in PrP-CAA (Q160X) were visually identified from the reference 2D class averages. For PrP-CAA (Q160X) PHFs and SFs, a new 300-pixel box size without downscaling was used to re-extract with inter-box distance of approximately 15 Å. A box size of 320 pixels was used for GSS (F198S). At this stage, multiple rounds of reference-free 2D classification were carried out to discard suboptimal 2D class averages. The initial 3D reference maps were reconstructed de novo from best 2D class averages of comprising a full helical crossover. The initial round of 3D classification was low-pass-filtered to 60 Å. Several rounds of 3D classification were carried out to remove segments leading to suboptimal 3D class averages with regularization value $T = 20$, total classes $K = 4$. The final selected segments were used for final 3D auto-refinement with optimization of the helical twist and rise to yield 3D map showing clearly visible beta-strand separation and side-chain densities. We used a 10% helical z percentage parameter for post-reconstruction application of helical symmetry. The final reconstructions were sharpened using the standard post-processing procedures in RELION. The RELION helix toolbox was used to improve helical symmetry. Optimized twist and rise parameters for PrP-CAA (Q160X) PHFs, PrP-CAA (Q160X) SFs, and GSS (F198S) PHFs are 4.77 Å and − 1.2°, 4.79 Å and − 1.07°, and 4.85 Å and − 1.23°, respectively. Finally, the overall resolution was calculated from Fourier shell correlations at 0.143 between two independently refined half-maps, employing phase randomization for the convolution effects correction of an optimized, soft-edged solvent mask as implemented in the trueFSC.py program of our *jspr* software [57].

Model building

The previously deposited structure of PHF (PDB 5O3L) was fitted into the sharpened PrP-CAA (Q160X) and GSS (F198S) PHF density maps using Chimera [47]. The same was done for PrP-CAA (Q160X) SF using the deposited structure of SF (PDB 5O3T). The most central chain of each model (e.g., chain E) was adjusted into the electron density of each map by hand in Coot [9]. Each model was then refined using Rosetta according to a previously established procedure [66].

Density map and atomic model analysis

For each unique type of filament, the two half-maps were separately sharpened, aligned, scaled, and matched to the same density level for comparison. If the density of a region was not present in one of the half-maps, it was considered noise and not included for final evaluation. Once noise-free density feature was determined in this process, the full dataset maps for PrP-CAA (Q160X) and GSS (F198S) PHFs were globally sharpened with PHENIX [40], aligned, oriented, scaled, and matched to the density of the corresponding AD PHF map (EMD-3741) for comparison. The PrP-CAA (Q160X) SF density map was also processed and compared against the AD SF (EMD-3743) map in a similar manner. The maps were compared at the full map level, dimer level, and the monomer level.

Data availability

Cryo-EM maps have been deposited in the Electron Microscopy Data Bank (EMDB) under accession numbers EMD-23871 for PrP-CAA (Q160X) PHF, EMD-23890 for PrP-CAA (Q160X) SF, and EMD-23894 for GSS (F198S) PHF case 1. Refined atomic models have been deposited in the Protein Data Bank (PDB) under accession numbers 7MKF for PrP-CAA (Q160X) PHF, 7MKG for PrP-CAA (Q160X) SF, and 7MKH for GSS (F198S) PHF case 1. The mass spectrometry proteomics data generated in this study have been deposited to the ProteomeXchange Consortium [61] via the PRIDE partner repository [46] with the dataset identifier PXD025663. Whole-exome sequencing data have been deposited in the National Institute on Aging Alzheimer's Disease Data Storage Site (NIAGADS; https://www.niagads.org), under accession number ng00107.

Results

Tau aggregates in Prion-Protein Amyloidoses are composed of hyperphosphorylated Tau containing three- and four-repeat Tau isoforms

One of the hallmarks of the neuropathology of PrP-CAA (Q160X) and GSS (F198S) is the co-existence of APrP and Tau deposits (Fig. 1, Figure S1). Severe Tau neurofibrillary pathology including NFTs and neuropil threads (NTs) in gray structures of the cerebrum and brainstem coexist in the same anatomical areas with APrP deposition. While APrP pathology is severe in the molecular and granule cell layers of the cerebellar cortex, there is no Tau

deposition in any of the cerebellar compartments in either of the two diseases. In PrP-CAA (Q160X), APrP angiopathy coexists with severe limbic and neocortical Tau pathology that, as in GSS (F198S), is also characterized by the presence of numerous NFTs and NTs, that are decorated using antibodies recognizing hyperphosphorylated Tau and 3R- and 4R-Tau (Figure S1). APrP fibrillary deposits are decorated by antibodies recognizing PrP and visualized within vessel walls and intimately adherent to them, often forming rosary-like structures. APrP angiopathy involves the walls of small- and medium-sized parenchymal and

leptomeningeal blood vessels. In GSS (F198S), NFTs and NTs are decorated using antibodies recognizing hyperphosphorylated Tau, 3R- and 4R-Tau (Figure S1). Tau deposits are seen in neuronal perikarya, in NTs, and in the processes that surround PrP plaques (Fig. 1, Figure S1). PrP plaques may be diffuse or have cores (unicentric or multicentric plaques) that are predominantly in layers 1, 4, 5, and 6 of frontal, insular, temporal, and parietal cortices. It is noteworthy that Tau pathology is equally severe in PrP-CAA (Q160X) and GSS (F198S), even though the APrP pathology is localized in different compartments:
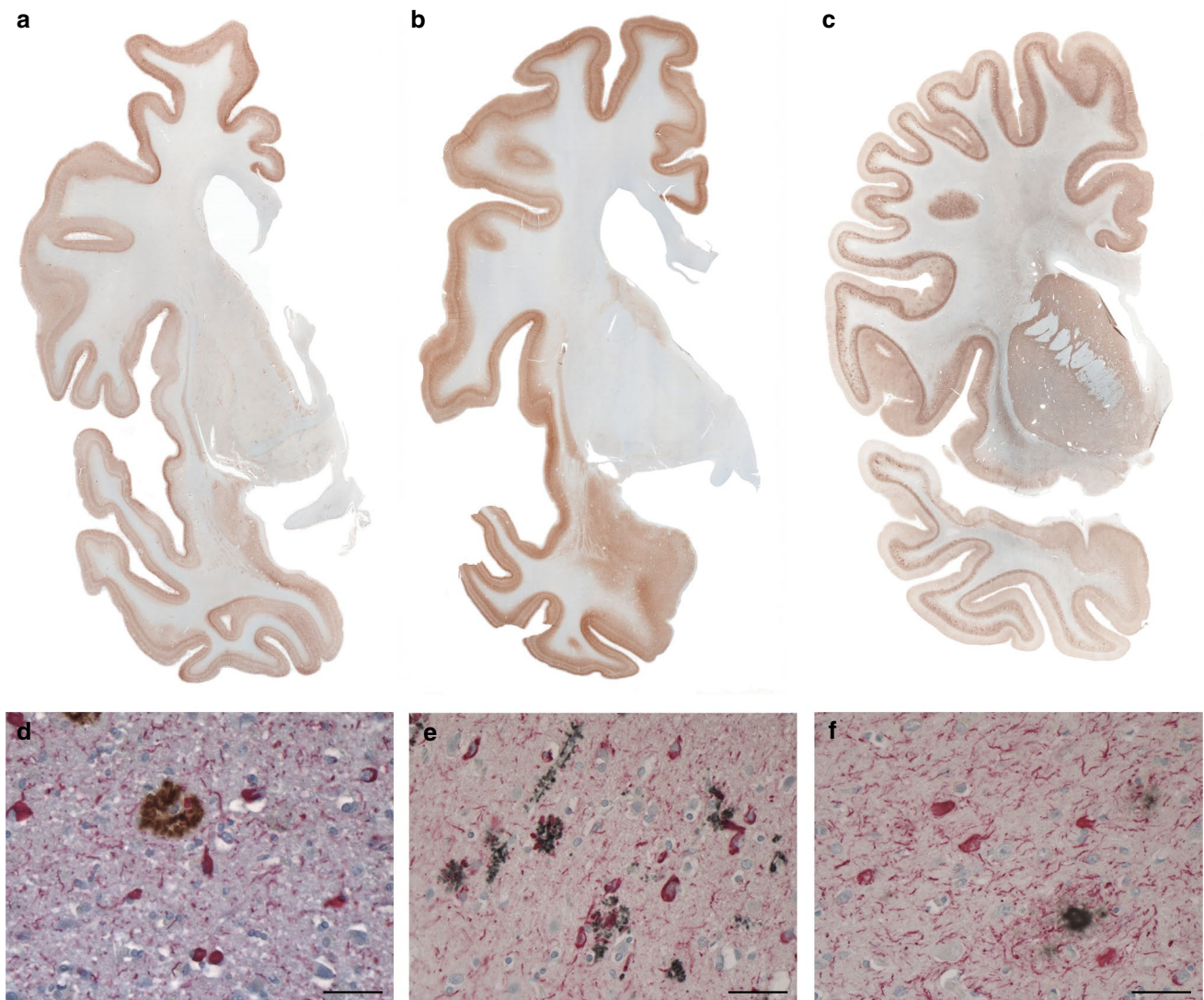
Fig. 1 *Immunohistochemistry in PrP-CAA (Q160X) and GSS (F198S) compared to AD.* Hemispheric coronal sections show the distribution of Tau pathology at the level of the cerebral cortex, caudate nucleus and putamen in a case of AD (Case 1, **a**), cerebral cortex, amygdala, and caudate nucleus in PrP-CAA (Q160X) **b**, and cerebral cortex, caudate nucleus, putamen, and claustrum in GSS (F198S) (Case 1, **c**). Double immunohistochemistry of Tau and Aβ in AD (**d**), Tau and PrP in PrP-CAA (Q160X) (**e**), and Tau and PrP in GSS (F198S) (**f**). Nerve cell bodies and NTs are reactive for Tau (red) and are seen in the vicinity of parenchymal Aβ plaques (brown) in AD (**d**), blood vessels with APrP angiopathy (black) in PrP-CAA (Q160X) (**e**), or parenchymal APrP plaques (black) in GSS (F198S) (**f**). **a–f**, Anti-Tau antibody AT8; **d** Anti-Aβ antibody NAB 228; **e**, **f** Anti-PrP antibody 95–108. Scale bar, 50 μm

i.e., blood vessels walls in PrP-CAA (Q160X) versus neuropile in GSS (F198S).

Western blot analysis of sarkosyl-insoluble fractions shows the presence of Tau bands with a migration pattern indistinguishable from that seen in AD (Fig. 2, Figure S2a). Western blot analysis also shows that APrP does not co-purify with Tau in our Tau preparations (Fig. 2a). The purified sarkosyl-insoluble fraction enriched for Tau aggregates induces Tau aggregation in a biosensor cell system derived by transducing HEK293T cells with 2 separate lentiviral constructs encoding Tau RD P301S-CFP and Tau RD P301S-YFP [18, 33]. Tau isolated from the frontal cortex of PrP-CAA (Q160X) and GSS (F198S) leads to the formation of aggregates similar to those from Tau isolated from AD brains (Fig. 2b). Aggregation is not seen in samples prepared from frontal cortex (FC) from controls nor from the cerebellum (CB) of PrP-CAA (Q160X) and GSS (F198S) patients, where PrP pathology is severe, but Tau aggregates are not detected.

The sarkosyl-insoluble fraction enriched in Tau aggregates from PrP-CAA (Q160X) and GSS (F198S) was incubated in the presence or absence of pronase and evaluated by a dot-blot assay using a variety of antibodies against different epitopes of Tau protein (Figure S2a). We compared the susceptibility of the Tau preparation to pronase digestion in the two diseases to that of Tau fibrils isolated from AD, CTE, CBD, and PiD. Digestion with pronase removes the epitopes recognized by the BR133, HT7 and AT8 antibodies, located in the N-terminal portion of the molecule. It also removes the epitope recognized by the BR134 antibody, located in the C-terminus of Tau. Both N- and C-terminal portions of Tau are also referred to as the "fuzzy coat" [68]. Interestingly, the epitope recognized by the BR135 antibody is partially resistant to pronase digestion, suggesting that this sequence is part of the filament core as in AD, CTE, CBD, and PiD (Figure S2b) [10–12, 16, 64].

Analysis of dispersed preparations of Tau filaments by transmission electron microscopy (TEM) suggests that Tau aggregates from GSS (F198S) may be composed predominantly of paired helical filaments (PHFs) that appear to be identical to those seen in AD (Figure S2c). In PrP-CAA (Q160X), we estimate a ratio of ~4:1 PHFs to straight filament (SFs), while SFs could not be detected in the three different GSS (F198S) cases analyzed, suggesting that PHFs may be the predominant (if not the only) type of filaments in GSS (F198S). Using antibodies against different epitopes of Tau protein (Figure S2a) in immuno-EM, we observe that Tau filaments in PrP-CAA (Q160X) and GSS (F198S) are composed of full-length, hyperphosphorylated Tau. Immuno-EM analysis of Tau fibrils after pronase digestion shows that the cores of Tau filaments in PrP-CAA (Q160X) and GSS (F198S) share epitopes located in the R3 and R4 repeat domains. Treatment with pronase removes the fuzzy coat, composed of N- and C-terminal sequences, abolishing the positive labeling observed before pronase treatment. The epitope recognized by antibody BR135, which labels Tau on Western blots of dispersed filaments and in dot-blot analyses, is located in the core of Tau filaments, and is not accessible to the antibody before or after pronase treatment by immuno-EM (Figure S2c). These findings are consistent with the presence of the same Tau sequences in the core of Tau filaments in PrP-CAA (Q160X), GSS (F198S), and AD [11, 16].

Cryo-EM of Tau filaments in PrP-CAA (Q160X) and GSS (F198S)

We determine the structure of Tau filaments at high resolution by cryo-EM imaging and 3D reconstruction. We observe two types of Tau filaments within the sarkosyl-insoluble fraction of PrP-CAA (Q160X), similar to PHFs and SFs of AD (Fig. 3a,c). PHFs were ~70% and SFs were ~30% of the filament population, both composed of two protofilaments with C-shaped subunits (Figure S3) [16]. Two-dimensional classification readily separated PHF and SF for further processing (Fig. 3d,e). We determine the structure of PHFs and SFs in PrP-CAA (Q160X) using helical reconstruction in RELION3.1 to 3.0 Å resolution (Fig. 3a, c, f) (Table S1). The crossover distance for both types of filaments is approximately between 700 and 850 Å with a width of about 40–300 Å. In GSS (F198S), the protofilament organization of PHFs is identical to that of PrP-CAA protofilaments; however, protofilaments of SF were not visualized. Using helical reconstruction in RELION3.1, we determine a 3.2 Å resolution map of the ordered core of PHFs from GSS (F198S) (Fig. 3b, f), with the same crossover distance and width of PHFs from PrP-CAA (Q160X), and the same monomeric fold as the AD fold, i.e., the C-shaped unit (Figure S3).

The cores are composed of eight β-strands (Figure S3, S4a) adopting a C-shaped architecture that is perpendicular to the axial direction of the filament encompassing residues V_{306} to F_{378} of Tau in PrP-CAA (Q160X), and K_{274} to R_{379} of 3R Tau and S_{305} to R_{379} of 4R Tau in GSS (F198S) (Figure S3). The cores include residues located in the R3 and R4 repeat domains, with additional densities extending from the N- and C-terminal regions of the core (Figure S4a). The polar amino acids have side chains mostly facing the solvent (outside the protofilament core) and the non-polar amino acids like valine and isoleucine are facing inwards in the protofilament core forming hydrophobic patches (Fig. 4). PHFs and SFs in PrP-CAA (Q160X) and PHFs in GSS (F198S) have 8 β-strands that pack together to form the fold (Figure S3i-k). The β1 and β2 strands run anti-parallel to β8 (in a cross-β pattern), β3 runs anti-parallel to β7, and β4, β5 and β6 are arranged in a triangular fashion. In between the β-strands, glycine residues forming β-turns
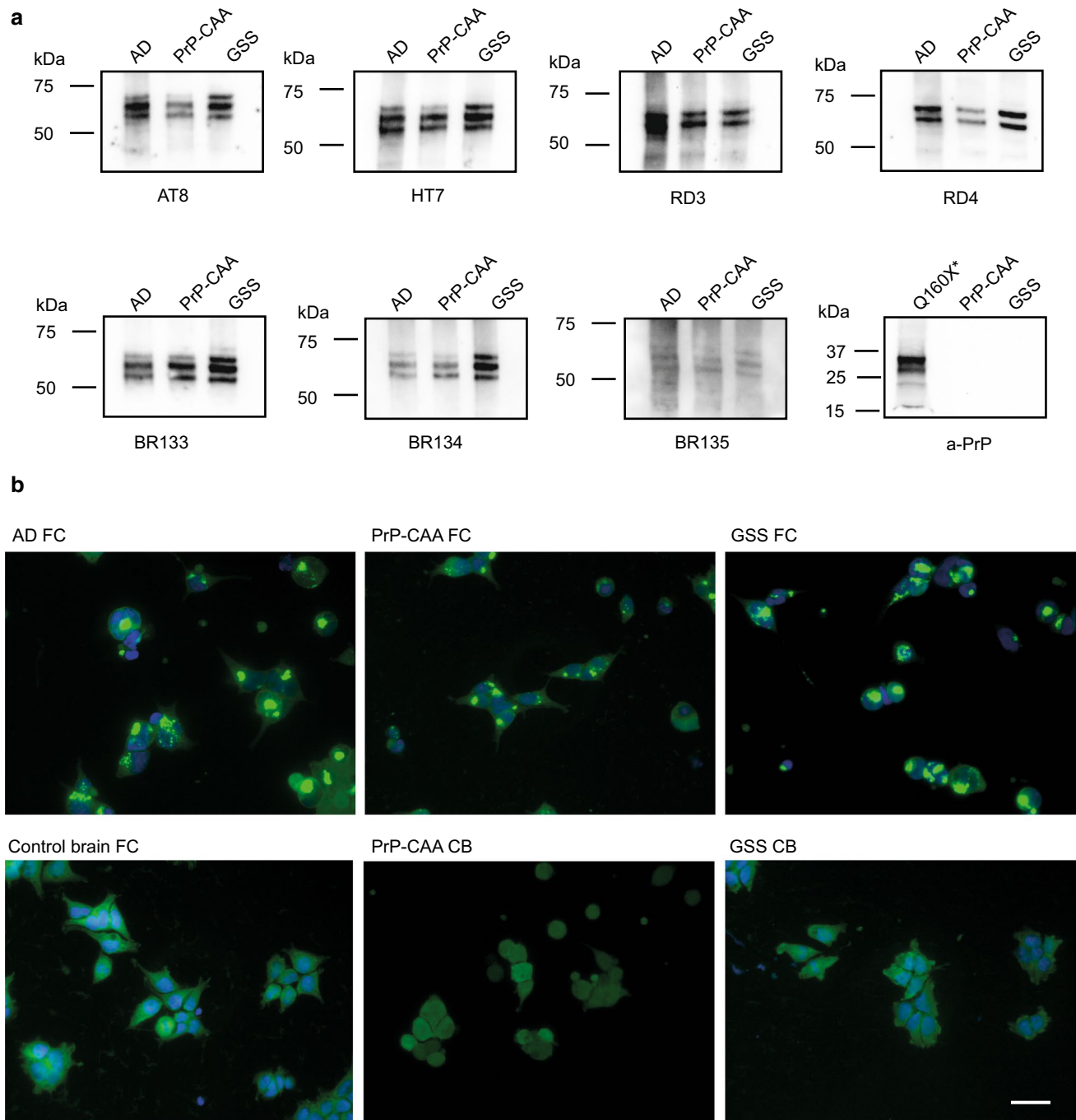
Fig. 2 *PrP-CAA (Q160X) and GSS (F198S) Tau are indistinguishable from AD Tau by Western blot or seeding assay.* Western blots of sarkosyl-insoluble Tau fractions from AD (Case 2), PrP-CAA (Q160X), and GSS (F198S) (Case 2) show that Tau aggregates consist of full length, hyperphosphorylated Tau with an identical electrophoretic pattern, consisting of major bands of 60, 64, and 68 kDa. No PrP immunoreactivity is seen in the sarkosyl-insoluble Tau fractions of PrP-CAA (Q160X) and GSS (F198S). Total brain homoge-

nate from PrP-CAA (Q160X*) was used as positive control for PrP (**a**). Tau biosensor cells incubated with the sarkosyl-insoluble fraction obtained from frontal cortex (FC) of AD (Case 2), PrP-CAA (Q160X) and GSS (F198S) (Case 2) show Tau seeding activity, whereas the insoluble fraction of FC from control brain, and cerebellum (CB) from PrP-CAA (Q160X) and GSS do not seed Tau aggregation in vitro (**b**). Scale bar: 20 μm

and proline residues breaking the β-strands reduce the stress of having 8 β-strands in one protofilament core (Fig. 4). Ordered in-register H-bonding between the residues in the

β-strands further reduce this stress. The residues in β1 are mostly hydrophobic, packing with the last few residues of β8 strand (L_{376} and F_{378}). Contrary to that, the polar residues
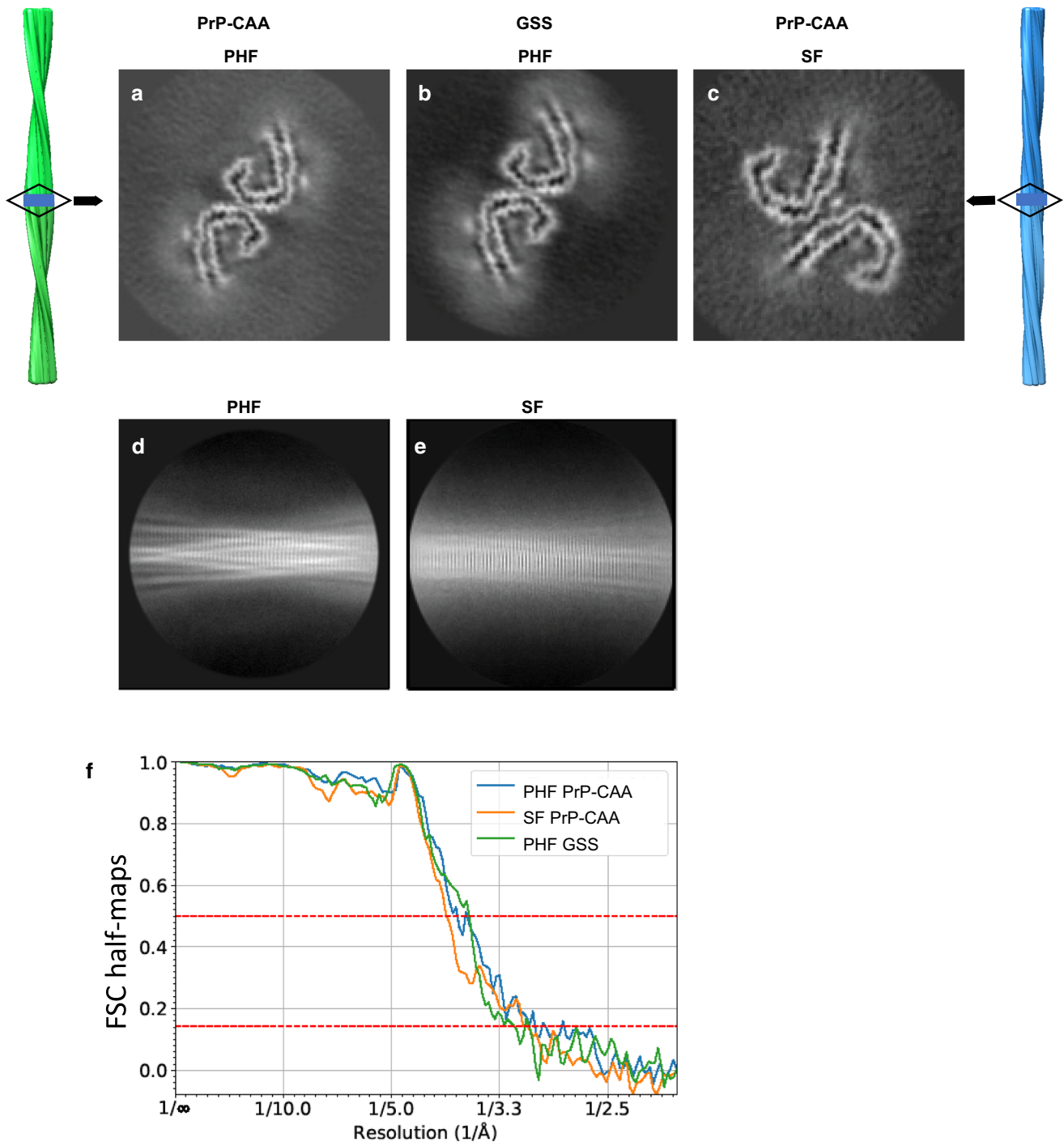
Fig. 3 *Cryo-EM reconstructions of PHF and SF from PrP-CAA (Q160X) and PHF from GSS (F198S).* The structures show identical pairs of C-shaped protofilaments and the same inter-protofilament packing between PHFs (**a**, **b**) but different packing for SFs (**c**). The rectangular boxes in the vertical, surface view of the helical recon- structions of PHFs (left, green), and SFs (right, blue) show the loca- tion of the cross-sectional densities (**a**–**c**). 2D class averages of PHF (**d**) and SF (**e**) of PrP-CAA (Q160X). Fourier Shell Correlation (FSC) curves for independently refined half-maps of PrP-CAA (Q160X) PHFs and SFs, and GSS (F198S) PHFs (**f**)

in the β2 strand are facing inwards to interact with the polar residues of the β8 strand (Figure S3, Fig. 4). A β-turn consisting of G_{323} and G_{326} separates the β2 and β3 strands and provides a 90degree turn to the core. The β3 strand is followed by the $_{332}$PGGG motif that forms an interface with the other protofilament forming a PHF (Figure S4b) and provides another turn in the core structure. V_{337} and V_{339} from the β4 strand interact with I_{354} of the β6 strand and L_{357} of
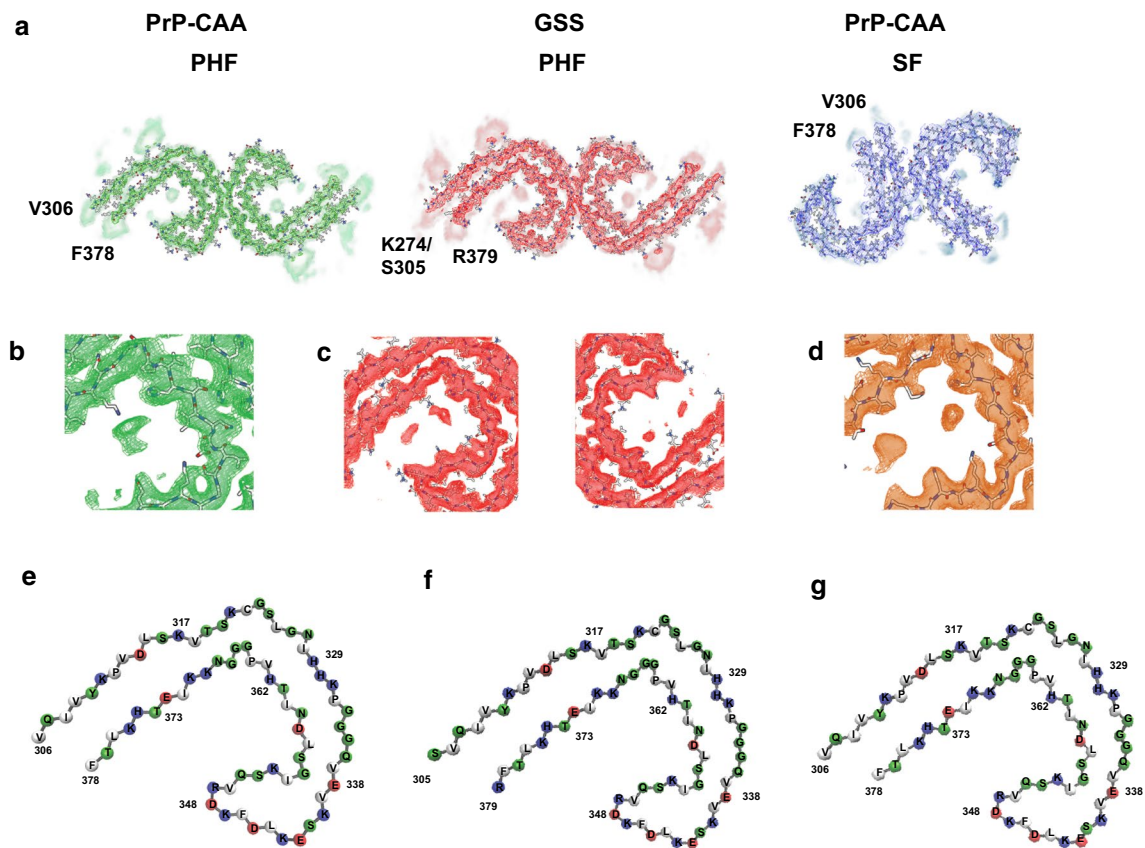
Fig. 4 *Cryo-EM densities and atomic models of PHFs and SFs.* Sharpened, high-resolution maps are shown in green (PHF, PrP-CAA (Q160X)), red (PHF, GSS (F198S)), and blue (SF, PrP-CAA (Q160X)). The blurred map regions represent extra densities low-pass-filtered to 5 Å (**a**). PrP-CAA (Q160X) PHF extra density (**b**) and GSS (F198S) extra density (**c**) around the core have different locations and orientations to that of the extra density of AD PHF (**d**). Schematic view of the PrP-CAA (Q160X) (**e**) and GSS (F198S) (**f**) PHF protofilament cores compared to AD (**g**) PHF (PDB: 5o3l) showing the similarities in the folds. The colors represent the polarity of the amino acids (red: negatively charged, blue: positively charged, white: non-polar)

β7 strand to form another hydrophobic patch. The β4–β6 strands form a β-helix-like configuration where the three strands form a triangle-like structure (Fig. 4, Figure S3). The inside of the β-helix is filled with hydrophobic amino acid side chains (V_{339}, L_{344}, F_{346}, V_{350}, and I_{354}). The side chains of the polar amino acids are facing outwards and they are mostly alternatively charged. E_{342}–K_{343} and K_{347}–R_{349} residues form the two corners of the triangle. G_{355} provides the turn between β6 and β7 strands. The β7 and β8 strands are interspersed by the $_{364}$PGGG motif that provides the 90 degree turn between them. PHFs and SFs differ in how the two C-shaped protofilaments interact with each other (Fig. 4, Figure S4b). In PHFs, the two protofilaments are related by a 2_1 screw symmetry with only a small shift (~ 2.4 Å) along the filament axis, which results in the two C-shaped subunits appearing to be inverted and symmetrically interacting with each other (Fig. 4). The interface between protofilaments (Figure S4b) is formed by the anti-parallel stacking of residues P_{332} to Q_{336}, with the G residues 333 to 335 forming

H-bondings, and two additional H-bonds between Q_{336} and K_{331} from the opposite protofilament. The protofilament surface of PrP-CAA (Q160X) and GSS (F198S) PHFs is similar to the filament surface of PHFs in AD (Figure S4B). The two protofilaments in SF structures are asymmetrically arranged. In SFs, the sidechains of residues P_{312}–K_{321} of one protofilament are in close proximity with the sidechains of the residues K_{317}–S_{324} of the other protofilament, while the surface between the two protofilaments is not stabilized by H-bonds like in PHFs.

Additional densities exist around the protofilament core

We observe additional densities around the protofilament cores (Figs. 3, 4). As illustrated in Fig. 4 by the low-pass filtered density map, both N- and C-termini of the cores have disordered densities. In the cores of PHFs in PrP-CAA (Q160X) and GSS (F198S), the sidechains of K_{317}, T_{319} and

K_{321} interact with an additional density outside the core. Similarly, this strong additional density is seen in the SFs of PrP-CAA (Q160X) at the protofilament interface. Fitzpatrick et al. [5] hypothesized these additional densities to be the $_7EFE_9$ motif at the N-terminus of the Tau protein and proposed that the formation of salt bridges stabilized the interaction between two SF protofilaments. To further investigate the extra densities seen near residues within the core of Tau PHFs and SFs, we perform mass spectrometry (MS) on Tau filaments from AD, PrP-CAA (Q160X) and GSS (F198S). We achieve 100% coverage of the core region of filaments from all 3 diseases. We determine Tau filaments in each disease to be highly post-translationally modified, especially in respect to phosphorylation, acetylation, ubiquitination, and deamidation (Table S3). Specifically, we find peptides in which K_{317} is ubiquitinated in Tau filaments from all 3 diseases, which may correlate to the large extra density near this residue in both PHFs and SFs, therefore suggesting that ubiquitination of K_{317} may also contribute to SF stabilization. A density present near residues I_{371} and T_{373} in PHFs and SFs in AD is not present in Tau filaments from PrP-CAA (Q160X) (Fig. 4) nor do we find any PTMs on these residues via MS (Table S3). In addition, a density that interacts with the H_{362} residue side-chain in Tau filaments in AD is seen to interact with the side-chain of K_{369} in Tau filaments from PrP-CAA (Q160X) and GSS (F198S) (Fig. 4). In fact, our MS results determine that K_{369} is acetylated in both AD and PrP-CAA (Q160X), whereas no PTMs are observed on H_{362}, suggesting that this extra density may be interacting with K_{369} as opposed to H_{362}. Interestingly, Tau in GSS (F198S) seems to be less phosphorylated at serine residues (S_{320}, S_{324} and S_{356}) located in the R3 and R4 region than in Tau filaments from AD and PrP-CAA (Q160X) (Table S3).

Discussion

PrP-CAA (Q160X) and GSS (F198S) are two Prion-Protein Amyloidoses that have distinct clinical and neuropathologic phenotypes. They differ significantly from Creutzfeldt–Jakob disease (CJD), the most common form of prion disease [22]. PrP-CAA (Q160X) and GSS (F198S) are caused by mutations in the *PRNP* gene that lead to APrP formation and deposition in the vascular compartment in PrP-CAA (Q160X) and in the brain parenchyma in GSS (F198S) [21, 23, 37]. Interestingly, both conditions are neuropathologically characterized by the presence of Tau aggregates. Western blot of Tau aggregates from PrP-CAA (Q160X), GSS (F198S), and AD show identical pattern of migration and immunoreactivity using antibodies against 3R- and 4R-au, strongly suggesting that Tau aggregates in PrP-CAA (Q160X) and GSS (F198S) are composed by 3R- and 4R-au isoforms. By TEM of negative stained preparations, Tau aggregates in

PrP-CAA (Q160X) are found to be composed of PHFs and SFs, while in GSS (F198S) Tau aggregates are found to be predominantly, if not entirely, composed of PHFs. Analysis by immuno-EM coupled to pronase treatment suggests that the core of the Tau filaments in PrP-CAA (Q160X) and GSS (F198S) contains the R3 and R4 repeats, as in AD. By cryo-EM, PHFs and SFs are found to be made of two protofilaments with a common cross-β/β-helix C-shaped architecture, as in AD [11, 16]. The core encompasses residues V_{306} to F_{378} of Tau in PrP-CAA (Q160X), and K_{274} to R_{379} of 3R Tau and S_{305} to R_{379} of 4R-Tau in GSS (F198S), with disordered densities sensitive to pronase degradation extending from the N- and C- termini. This is similar to the recently reported high-resolution cryo-EM structures of PHFs and SFs from AD, with R_{379} and E_{380} from the sequence after R4 at the C-terminus, and G_{304} and S_{305} from R2 in 4R Tau, and G_{273} and K_{274} from R1 in 3R-Tau at the N-terminus [11]. Additional densities are identified near the core of Tau filaments from PrP-CAA (Q160X) and GSS (F198S), specifically at the sidechains of K_{317}, T_{319}, and K_{321}. By mass spectrometry analysis, we establish the presence of extensive PTMs in Tau aggregates from PrP-CAA (Q160X) and GSS (F198S). We observe K_{317} to be ubiquitinated in AD, PrP-CAA (Q160X) and GSS (F198S), suggesting that the extra densities observed by cryo-EM near this residue in PrP-CAA (Q160X) and GSS (F198S) correspond to ubiquitination at this lysine. We also observe PTMs that have been reported to be important in Tau fibrillization and propagation in AD [27, 28], for example, phosphorylation at T_{231}, thought to be central to the initial steps of Tau detachment from microtubules and subsequent aggregation [1, 2], is found in our cases of AD, PrP-CAA (Q160X) and GSS (F198S). We also observe PTMs within the two hexapeptide motifs, $_{275}VQIINK_{280}$ and $_{306}VQIVYK_{310}$, which are known to be the minimum required motifs for Tau protein aggregation [39]. By MS, we observe that Tau from PrP-CAA (Q160X) is phosphorylated at S_{199} and S_{202}, while Tau from GSS (F198S) is phosphorylated at S_{202}; however, Tau deposits were immunoreactive for the AT8 phosphoepitope (phosphorylation at residues S_{202} and T_{205} but also other epitopes, including S_{199} and S_{208}) [41] by immunohistochemistry, immunoblotting, and immuno-EM methods. PHF-1 also decorates Tau aggregates in PrP-CAA (Q160X) and GSS (F198S) (not shown), and by MS, we are able to detect the phosphorylated residues S_{396} and S_{404}, which constitute the epitope recognized by antibody PHF-1 (directed against the doubly phosphorylated epitope S_{396} and S_{404}) [29, 32]. The MS data also show deamidation of N_{279}, which has been suggested to contribute to the AD folds as opposed to the folds seen in CBD [3, 7]. However, we observe deamidation at this residue only in AD and PrP-CAA (Q160X), but not in GSS (F198S) tryptic peptides, suggesting that this PTM may contribute to PHF over SF formation, and offer explanation as to the lack of

SFs in GSS (F198S). In addition, we observe phosphorylation at T_{175} and S_{237} in all three diseases. It has recently been reported that singly and doubly ubiquitinated peptides at residues K_{311} and K_{317} and phosphorylation at T_{217} and S_{262} may differentiate between AD and control groups [67]. We find that all these residues are post-translationally modified in PrP-CAA (Q160X) and GSS (F198S). We observe peptides containing K_{311} to be either ubiquitinated or acetylated, while K_{317} is always found ubiquitinated. Although we do not find changes in K_{280}, PTMs in K_{280} and K_{311} have been shown to regulate Tau fibrillization in vitro [62]. It has been previously suggested that extra densities near K_{317} and K_{321} of AD and CTE Tau may be formed by the $_7EFE_9$ motif of Tau, which may stabilize the protofilament interface of SFs [12, 16]. We identify ubiquitination of K_{317} in PrP-CAA (Q160X) and GSS (F198S) Tau, suggesting ubiquitin at this site as another possible explanation for the extra density seen via cryo-EM. Additional reports have suggested that ubiquitination of K_{311} and K_{317} of the core of Tau filaments would lead to SF formation, rather than PHF [7]; however, our data show that despite ubiquitination at K_{311} and K_{317} of tryptic peptides from GSS (F198S), no SFs are found within GSS (F198S) Tau filaments. In addition, we do not find peptides phosphorylated at S_{320}, S_{324} and S_{356} in GSS (F198S), which are located in the R3 and R4 region and are phosphorylated in AD and PrP-CAA (Q160X). Our data suggest that these specific PTMs may not be critical for SF formation, and that PTMs may not fully mediate the structural diversity seen between Tau filaments from different diseases. Phosphorylation at T_{175}, S_{237}, and ubiquitination at K_{281}, have been associated with symptomatic AD at Braak VI stage [5, 67]

Amyloid and Tau aggregates coexist in AD and in other diseases in addition to the group of the PrP Amyloidoses [22], two of which are reported here. In fact, in other hereditary cerebral amyloid diseases such as Familial British dementia (FBD) [34, 59] and Familial Danish dementia (FDD) [35, 60], a severe neurofibrillary Tau pathology occurs. Our study shows for the first time that Tau fibrils deposited in the brain of individuals with a brain amyloidosis other than AD are biochemically, antigenically, and structurally identical. Moreover, a recent study shows that Tau fibrils isolated from the brain of individuals with FBD and FDD are also structurally identical to those in AD [56]. The co-existence of Tau aggregates with different types of amyloids suggests a common mechanism through which amyloids, whether Aβ in AD, APrP in Prion diseases, ABri in FBD or ADan in FDD, trigger aggregation of Tau, resulting in Tau filaments with identical structure at their core (Fig. 5). Furthermore, Tau from the brains of patients with AD, GSS (F198S), and PrP-CAA (Q160X) have similar seeding activities in vitro, as has been also seen for brain homogenates from AD and PART [38]. For AD, it has been proposed that Aβ provides a crucial element toward Tau
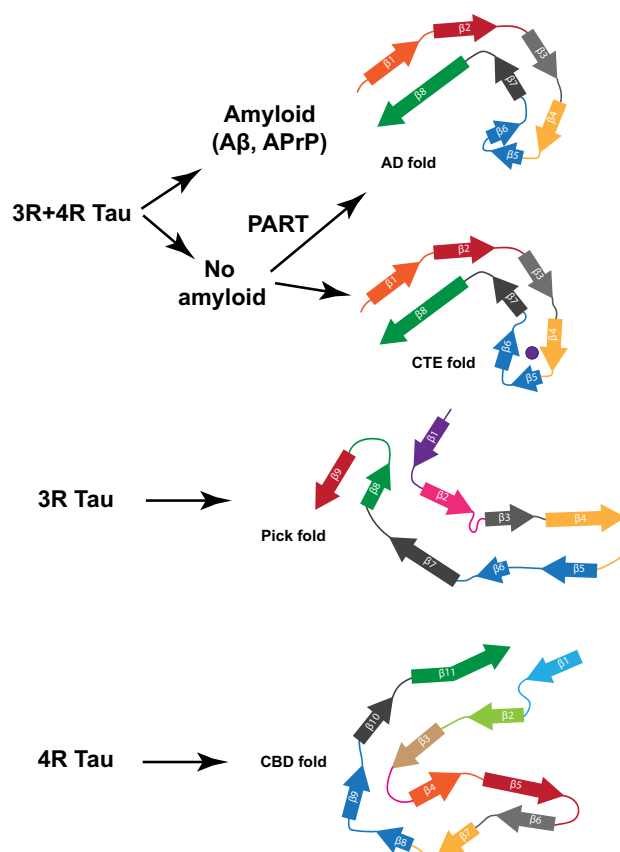
Fig. 5 *Different folds of Tau that have been identified to-date*. Two different Tau folds are associated with 3R and 4R-Tau and make the Tau aggregates in AD, PrP-CAA (Q160X), GSS (F198S), PART, and CTE. A Tau fold associated with 3R-Tau makes the inclusions of Pick disease and a Tau fold associated with 4R-Tau makes the aggregates in CBD. Among the four folds, one known as the Alzheimer Tau fold can occur in the presence or in the absence of an extracellular amyloid deposition. Analysis of additional diseases characterized by 3R-, 4R-, and 3R and 4R-Tau will determine whether this is the complete Tau fold landscape or if additional folds may be found associated with different diseases

aggregation [4, 30]. This hypothesis has been supported by genetic forms of AD due to mutations in the *AβPP*, *PSEN1*, and *PSEN2* genes that consistently alter the metabolism of Aβ, with a consequent Tau hyperphosphorylation and formation of Tau aggregates in vitro and in vivo [15, 19, 28]. Altered Tau metabolism in association with APrP has also been observed in in vitro studies [42] and in vivo in mouse models [48, 50]. By determining the structure of the core of Tau filaments from diseases caused by two distinct *PRNP* mutations, F198S and Q160X, to be identical to the core of Tau filaments from AD, we uncover potential links between amyloid proteins and the resulting Tau aggregation. Structural data are urgently needed for the identification of specific ligands for in vivo imaging of Tau aggregates in a wide range of neurodegenerative diseases.

Declarations

References

1. Alonso AD, Di Clerico J, Li B, Corbo CP, Alaniz ME, Grundke-Iqbal I et al (2010) Phosphorylation of Tau at Thr212, Thr231, and Ser262 combined causes neurodegeneration. J Biol Chem 285(40):30851–30860

2. Alquezar C, Arya S, Kao AW (2021) Tau post-translational modifications: dynamic transformers of tau function, degradation, and aggregation. Front Neurol 11:595532

3. Arakhamia T, Lee CE, Carlomagno Y, Duong DM, Kundinger SR, Wang K et al (2020) Posttranslational modifications mediate the structural diversity of tauopathy strains. Cell 180(4):633–644

4. Beyreuther K, Masters CL (1991) Amyloid precursor protein (APP) and beta A4 amyloid in the etiology of Alzheimer's disease: precursor-product relationships in the derangement of neuronal function. Brain Pathol 1(4):241–251

5. Braak H, Braak E (1991) Neuropathological staging of Alzheimer-related changes. Acta Neuropathol 82(4):239–259

6. Crary JF, Trojanowski JQ, Schneider JA, Abisambra JF, Abner EL, Alafuzoff I et al (2014) Primary age-related tauopathy (PART): a common pathology associated with human aging. Acta Neuropathol 128:755–766. https://doi.org/10.1007/s00401-014-1349-0

7. Dan A, Takahashi M, Masuda-Suzukake M, Kametani F, Nonaka T, Kondo H et al (2013) Extensive deamidation at asparagine residue 279 accounts for weak immunoreactivity of tau with RD4 antibody in Alzheimer's disease brain. Acta Neuropathol Commun 1(1):54. https://doi.org/10.1186/2051-5960-1-54

8. Duyckaerts C, Braak H, Brion JP, Buée L, Del Tredici K, Goedert M et al (2015) PART is part of Alzheimer disease. Acta Neuropathol 129(5):749–756

9. Emsley P, Lohkamp B, Scott WG, Cowtan K (2010) Features and development of *Coot*. Acta Cryst D66:486–501

10. Falcon B, Zhang W, Murzin AG, Murshudov G, Garringer HJ, Vidal R et al (2018) Structures of filaments from Pick's disease reveal a novel tau protein fold. Nature 561(7721):137–140

11. Falcon B, Zhang W, Schweighauser M, Murzin AG, Vidal R, Garringer HJ et al (2018) Tau filaments from multiple cases of sporadic and inherited Alzheimer's disease adopt a common fold. Acta Neuropathol 136(5):699–708

12. Falcon B, Zivanov J, Zhang W, Murzin AG, Garringer HJ, Vidal R et al (2019) Novel tau filament fold in chronic traumatic encephalopathy encloses hydrophobic molecules. Nature 568(7752):420–423

13. Farlow MR, Murrell J, Ghetti B, Unverzagt F, Zeldenrust S, Benson M (1994) Clinical characteristics in a kindred with early-onset Alzheimer's disease and their linkage to a G→T change at position 2149 of the amyloid precursor protein gene. Neurology 44(1):105–111

14. Farlow JL, Robak LA, Hetrick K, Bowling K, Boerwinkle E, Coban-Akademir ZH et al (2016) Whole-exome sequencing in familial Parkinson disease. JAMA Neurol 73:68–75

15. Ferrari A, Hoerndli F, Baechi T, Nitsch RM, Götz J (2003) beta-Amyloid induces paired helical filament-like tau filaments in tissue culture. J Biol Chem 278(41):40162–40168

16. Fitzpatrick AWP, Falcon B, He S, Murzin AG, Murshudov G, Garringer HJ et al (2017) Cryo-EM structures of tau filaments from Alzheimer's disease. Nature 547(7662):185–190

17. Fong JC, Rojas JC, Bang J, Legati A, Rankin KP, Forner S et al (2017) Genetic prion disease caused by PRNP Q160X mutation presenting with an orbitofrontal syndrome, cyclic diarrhea, and peripheral neuropathy. J Alzheimers Dis 55(1):249–258

18. Furman JL, Holmes BB, Diamond MI (2015) Sensitive detection of proteopathic seeding activity with FRET flow cytometry. J Vis Exp 106:e53205

19. Geula C, Wu CK, Saroff D, Lorenzo A, Yuan M, Yankner BA (1998) Aging renders the brain vulnerable to amyloid beta-protein neurotoxicity. Nat Med 4(7):827–831

20. Ghetti B, Oblak AL, Boeve BF, Johnson KA, Dickerson BC, Goedert M (2015) Frontotemporal dementia caused by *microtubule-associated protein tau* gene (MAPT) mutations: a chameleon for neuropathology and neuroimaging. Neuropathol Appl Neurobiol 41(1):24–46

21. Ghetti B, Piccardo P, Spillantini MG, Ichimiya Y, Porro M, Perini F et al (1996) Vascular variant of prion protein cerebral amyloidosis with tau positive neurofibrillary tangles: the phenotype of the stop codon 145 mutation in PRNP. Proc Natl Acad Sci USA 93(2):744–748

22. Ghetti B, Piccardo P, Zanusso G (2018) Dominantly inherited prion protein cerebral amyloidoses - a modern view of Gerstmann–Sträussler–Scheinker. In: Pocchiari M, Manson J (eds) Handbook of clinical neurology, Elsevier, Amsterdam, Vol 153, pp 243–269

23. Ghetti B, Tagliavini F, Masters CL, Beyreuther K, Giaccone G, Verga L, et al (1989) Gerstmann-Sträussler-Scheinker disease. II. Neurofibrillary tangles and plaques with PrP-amyloid coexist in an affected family. Neurology 39(11):1453–1461

24. Goedert M, Eisenberg DS, Crowther RA (2017) Propagation of tau aggregates and neurodegeneration. Annu Rev Neurosci 40:189–210

25. Goedert M, Jakes R (1990) Expression of separate isoforms of human tau protein: correlation with the tau pattern in brain and effects on tubulin polymerization. EMBO J 9:4225–4230

26. Goedert M, Spillantini MG, Cairns NJ, Crowther RA (1992) Tau proteins of Alzheimer paired helical filaments: abnormal phosphorylation of all six brain isoforms. Neuron 8:159–168

27. Goedert M, Spillantini MG, Jakes R, Rutherford D, Crowther RA (1989) Multiple isoforms of human microtubule-associated protein tau: sequences and localization in neurofibrillary tangles of Alzheimer's disease. Neuron 3(4):519–526

28. Götz J, Streffer JR, David D, Schild A, Hoerndli F, Pennanen L et al (2004) Transgenic animal models of Alzheimer's disease and related disorders: histopathology, behavior and therapy. Mol Psychiatry 9(7):664–683

29. Greenberg SG, Davies P, Schein JD, Binder LI (1992) Hydrofluoric acid-treated tau PHF proteins display the same biochemical properties as normal tau. J Biol Chem 267:564–569

30. Hardy J, Allsop D (1991) Amyloid deposition as the central event in the aetiology of Alzheimer's disease. Trends Pharmacol Sci. 12(C):383–388

31. He S, Scheres SHW (2017) Helical reconstruction in RELION. J Struct Biol 198(3):163–176

32. Hoffmann R, Lee VMY, Leight S, Varga I, Otvos L Jr. (1997) Unique Alzheimer's disease paired helical filament specific epitopes involve double phosphorylation at specific sites. Biochemistry 36:8114–8124

33. Holmes BB, Furman JL, Mahan TE, Yamasaki TR, Mirbaha H, Eades WC et al (2014) Proteopathic tau seeding predicts tauopathy in vivo. Proc Natl Acad Sci USA 111(41):E4376-4385

34. Holton JL, Ghiso J, Lashley T, Rostagno A, Guerin CJ, Gibb G et al (2001) Regional distribution of amyloid-Bri deposition and its association with neurofibrillary degeneration in familial British dementia. Am J Pathol 158(2):515–526

35. Holton JL, Lashley T, Ghiso J, Braendgaard H, Vidal R, Guerin CJ et al (2002) Familial Danish dementia: a novel form of cerebral amyloidosis associated with deposition of both amyloid-Dan and amyloid-beta. J Neuropathol Exp Neurol 61(3):254–267

36. Hsiao K, Dlouhy SR, Farlow MR, Cass C, Costa MDa, Conneally PM, et al (1992) Mutant prion proteins in Gerstmann-Sträussler-Scheinker disease with neurofibrillary tangles. Nat Genet 1(1):68–71

37. Jayadev S, Nochlin D, Poorkaj P, Steinbart EJ, Mastrianni JA, Montine TJ et al (2011) Familial prion disease with Alzheimer disease-like tau pathology and clinical phenotype. Ann Neurol 69(4):712–720

38. Kaufman SK, Del Tredici K, Thomas TL, Braak H, Diamond MI (2018) Tau seeding activity begins in the transentorhinal/entorhinal regions and anticipates phospho-tau pathology in Alzheimer's disease and PART. Acta Neuropathol 136(1):57–67

39. Li W, Lee VM (2006) Characterization of two VQIXXK motifs for tau fibrillization in vitro. Biochemistry 45(51):15692–15701

40. Liebschner D, Afonine PV, Baker ML, Bunkóczi G, Chen VB, Croll TI et al (2019) Macromolecular structure determination using X-rays, neutrons and electrons: recent developments in Phenix. Acta Cryst D75:861–877

41. Malia TJ, Teplyakov A, Ernst R, Wu SJ, Lacy ER, Liu X et al (2016) Epitope mapping and structural basis for the recognition of phosphorylated tau by the anti-tau antibody AT8. Proteins 84(4):427–434

42. Matamoros-Angles A, Gayosso LM, Richaud-Patin Y, di Domenico A, Vergara C, Hervera A et al (2018) iPS Cell cultures from a Gerstmann-Sträussler-Scheinker patient with the Y218N PRNP mutation recapitulate tau pathology. Mol Neurobiol 55(4):3033–3304

43. McKee AC, Stern RA, Nowinski CJ, Stein TD, Alvarez VE, Daneshvar DH et al (2013) The spectrum of disease in chronic traumatic encephalopathy. Brain 136(Pt 1):43–64

44. Murrell J, Farlow M, Ghetti B, Benson MD (1991) A mutation in the amyloid precursor protein associated with hereditary Alzheimer's disease. Science 254(5028):97–99

45. Panegyres PK, Toufexis K, Kakulas BA, Cernevakova L, Brown P, Ghetti B, Piccardo P, Dlouhy SR (2001) A new PRNP mutation (G131V) associated with Gerstmann-Sträussler-Scheinker disease. Arch Neurol 58(11):1899–1902

46. Perez-Riverol Y, Csordas A, Bai J, Bernal-Llinares M, Hewapathirana S, Kundu DJ, et al (2019) The PRIDE database and related tools and resources in 2019: improving support for quantification data. Nucleic Acids Res. 8;47(D1):D442–D450

47. Pettersen EF, Goddard TD, Huang CC, Couch GS, Greenblatt DM, Meng EC et al (2004) UCSF Chimera—A visualization system for exploratory research and analysis. J Comput Chem 25:1605–1612

48. Piccardo P, King D, Brown D, Barron RM (2017) Variable tau accumulation in murine models with abnormal prion protein deposits. J Neurol Sci 383:142–150

49. Piccardo P, Langeveld JP, Hill AF, Dlouhy SR, Young K, Giaccone G et al (1998) An antibody raised against a conserved sequence of the prion protein recognizes pathological isoforms in human and animal prion diseases, including Creutzfeldt-Jakob disease and bovine spongiform encephalopathy. Am J Pathol 152(6):1415–1420

50. Race B, Phillips K, Kraus A, Chesebro B (2016) Phosphorylated human tau associates with mouse prion protein amyloid in scrapie-infected mice but does not increase progression of clinical disease. Prion 10(4):319–330

51. Risacher SL, Farlow MR, Bateman DR, Epperson F, Tallman EF, Richardson R et al (2018) Detection of tau in Gerstmann-Sträussler-Scheinker disease (PRNP F198S) by [18F]Flortaucipir PET. Acta Neuropathol Commun 6(1):114

52. Scheres SHW (2012) A Bayesian view on Cryo-EM structure determination. J Mol Biol 415(2):406–418

53. Schneider CA, Rasband WS, Eliceiri KW (2012) NIH Image to ImageJ: 25 years of image analysis. Nat Methods 9(7):671–675

54. Schwalbe M, Kadavath H, Biernat J, Ozenne V, Blackledge M, Mandelkow E et al (2015) Structural impact of Tau phosphorylation at Threonine 231. Structure 23(8):1448–1458

55. Shi Y, Murzin AG, Falcon B, Epstein A, Machin J, Tempest P et al (2021) Cryo-EM structures of tau filaments from Alzheimer's disease with PET ligand APN-1607. Acta Neuropathol 141(5):697–708

56. Shi Y, Zhang W, Yang Y, Murzin A, Falcon B, Kotecha A et al (2021) bioRxiv 2021.05.28.446130; doi: https://doi.org/10.1101/2021.05.28.446130

57. Sun C, Gonzalez B, Vago FS, Jiang W (2021) High resolution single particle Cryo-EM refinement using JSPR. Prog Biophys Mol Biol 160:37–42

58. Tran NH, Rahman MZ, He L, Xin L, Shan B, Li M (2016) Complete de novo assembly of monoclonal antibody sequences. Sci Rep 6(31730)

59. Vidal R, Frangione B, Rostagno A, Mead S, Révész T, Plant G et al (1999) A stop-codon mutation in the BRI gene associated with familial British dementia. Nature 399(6738):776–781

60. Vidal R, Révész T, Rostagno A, Kim E, Holton JL, Bek T et al (2000) A decamer duplication in the 3' region of the BRI gene originates an amyloid peptide that is associated with dementia in a Danish kindred. Proc Natl Acad Sci USA 97(9):4920–4925

61. Vizcaíno J, Deutsch E, Wang R et al (2014) ProteomeXchange provides globally coordinated proteomics data submission and dissemination. Nat Biotechnol 32:223–226

62. von Bergen M, Barghorn S, Li L, Marx A, Biernat J, Mandelkow EM et al (2001) Mutations of tau protein in frontotemporal dementia promote aggregation of paired helical filaments by enhancing local beta-structure. J Biol Chem 276(51):48165–48174

63. Zhang K (2016) Gctf: Real-time CTF determination and correction. J Struct Biol 193(1):1–12

64. Zhang W, Tarutani A, Newell KL, Murzin AG, Matsubara T, Falcon B et al (2020) Novel tau filament fold in corticobasal degeneration. Nature 580(7802):283–287

65. Zheng SQ, Palovcak E, Armache J-P, Verba KA, Cheng Y, Agard DA (2017) MotionCor2: anisotropic correction of beam-induced motion for improved cryo-electron microscopy. Nat Methods 14(4):331–332

66. Wang RY, Song Y, Barad BA, Cheng Y, Fraser JS, DiMaio F (2016) Automated structure refinement of macromolecular assemblies from cryo-EM maps using Rosetta. Elife 5:e17219

67. Wesseling H, Mair W, Kumar M, Schlaffner CN, Tang S, Beerepoot P et al (2020) Tau PTM Profiles Identify Patient Heterogeneity and Stages of Alzheimer's Disease. Cell 183(6):1699-1713.e13

68. Wischik CM, Novak M, Edwards PC, Klug A, Tichelaar W, Crowther RA (1988) Structural characterization of the core of the paired helical filament of Alzheimer disease. Proc Natl Acad Sci USA 85:4884–4888